Pulse-based state-of-charge and state-of-health estimation of randomly retired lithium-ion batteries for second-life applications

Citation for the original published paper (version of record):
Zhu, Q., Tao, S., Wik, T. (2026). Pulse-based state-of-charge and state-of-health estimation of randomly retired lithium-ion
batteries for second-life applications. Applied Energy, 426.
http://dx.doi.org/10.1016/j.apenergy.2026.128702

Applied Energy 426 (2026) 128702

Contents lists available at ScienceDirect

Applied Energy

journal homepage: www.elsevier.com/locate/apen

Pulse-based state-of-charge and state-of-health estimation of randomly retired lithium-ion batteries for second-life applications

Qingbo Zhu, Shengyu Tao*, Torsten Wik

Department of Electrical Engineering, Chalmers University of Technology, Hörsalsvägen 11, SE-412 96, Gothenburg, Sweden

HIGHLIGHTS

- Pulse tests enable joint SOC-SOH estimation without historical data.
- 21 pulse-response features capture SOC, degradation, and chemistry variations.
- TabPFN achieves mean absolute error down to 0.0076 for SOH and < 0.01 for SOC.
- Interpolation retains accuracy with 40%–70% reduction in SOC-dependent pulse tests.
- Framework enables fast, scalable screening of second-life batteries within the validated testing conditions.

ARTICLE INFO

Keywords:
State of health
State of charge
Pulse testing
Retired lithium-ion batteries
TabPFN
Reduced pulse testing

ABSTRACT

Retired lithium-ion batteries are an important resource for second-life energy storage, but their practical reuse requires rapid and efficient state assessment under unknown usage histories. To address this problem, we develop a pulse-based framework for joint state-of-health (SOH) and state-of-charge (SOC) estimation of randomly retired lithium-ion battery cells. A set of voltage-response features is extracted from short bipolar pulse tests and used as diagnostic descriptors. Based on these features, two machine learning models, extremely randomized trees (ExtraTrees) and a tabular prior-data fitted network (TabPFN), are employed for battery state estimation and evaluated using data from 270 retired cells that cover three chemistry types and four capacity classes. The results show that TabPFN clearly outperforms ExtraTrees and achieves mean absolute errors ranging from 0.0076 to 0.0306 for SOH estimation and below 0.01 for SOC estimation across all cell groups. To reduce the testing burden, a subset of SOC-dependent pulse tests is removed, and the missing feature points are reconstructed using interpolation methods. The reduced-test results show that near-baseline estimation accuracy can be retained even after removing 40%–70% of SOC-dependent pulse tests, depending on the target state and accuracy requirements. These results demonstrate a practical route toward faster, lower-cost, and scalable state assessment for second-life battery applications.

1. Introduction

The rapid growth of electric mobility is turning retired lithium-ion batteries into a major future resource stream for second-life energy storage. Global electric car sales exceeded 17 million in 2024 and reached 20.7 million in 2025 [1], while EV battery demand is projected to grow from about 1 TWh in 2024 to more than 3 TWh by 2030 [2]. A substantial fraction of these batteries will leave first-life service not because every cell is fully depleted, but because pack-level warranty limits, safety, performance, or imbalance constraints are no longer satisfied [3–5]. Many retired cells can still retain considerable usable capacity and may therefore be redirected to stationary storage, lower-power applications, or recycling pathways depending on their residual value. This emerging battery flow creates a major opportunity for circular energy storage.

Realizing this residual value requires fast and cost-effective state assessment before batteries can be safely handled, consistently tested, and routed to reuse or recycling [6]. Among the key state variables, state of charge (SOC) and state of health (SOH) are both indispensable. SOH determines residual capacity, economic reuse potential, and cell grouping for second-life assembly, whereas SOC affects handling, storage, and testing safety [7]. In practice, retired batteries usually arrive

* Corresponding author.
Email addresses: qingbo.zhu@chalmers.se (Q. Zhu), shengyu.tao@chalmers.se (S. Tao), tw@chalmers.se (T. Wik).

https://doi.org/10.1016/j.apenergy.2026.128702
Received 11 May 2026; Received in revised form 3 August 2026; Accepted 14 August 2026
Available online 24 August 2026

with unknown usage histories, uncertain charge states, and heterogeneous degradation conditions. Reliable estimation of both SOC and SOH is therefore essential for avoiding unsafe handling, inaccurate reuse decisions, and inefficient allocation of retired cells across second-life and recycling pathways.

In the absence of historical data, accurate SOH assessment of retired batteries has traditionally relied on full charge–discharge calibration, through which measured capacity provides a direct reference for residual health [8]. However, such protocols are difficult to scale because each cell must undergo controlled charging, resting, and discharging over an extended period, consuming both electrical energy and test-bench occupancy. This bottleneck becomes critical as the volume of retired batteries increases. To reduce the testing burden, a wide range of battery diagnosis methods has been developed, including equivalent-circuit models [9], electrochemical model-based approaches [10], incremental capacity [11] and differential voltage analysis [12], electrochemical impedance spectroscopy [13], and signatures from partial cycling [14]. These methods can provide valuable physical insights and, in some cases, shorter tests. Yet many still require well-controlled operating conditions, specialized instrumentation, sufficiently regular cycling data, or prior knowledge of battery history, which limits their direct use for randomly retired and heterogeneous batteries [15]. Recent advances in artificial intelligence and data-driven battery diagnostics have further expanded the possibilities for retired-battery assessment. Artificial-intelligence-based methods have been explored for battery reuse [16], recycling [17], and remanufacturing [18], supporting state diagnosis, sorting, lifetime prediction, and decision-making across the retired-battery value chain [19]. In addition, multi-scale unsupervised anomaly-detection frameworks have been developed for lithium-ion battery packs to identify abnormal cells or modules from operational data at different system levels [20].

Pulse-based techniques are attractive in this context because short current perturbations can probe resistance, polarization, and relaxation behavior from voltage responses using standard electrical measurements. Existing studies have used pulse responses for rapid retired-cell screening [21], fast capacity estimation [22,23], snapshot SOC identification [24], lifetime prognostics [25], and multi-aspect diagnostic assessment covering health, SOC, and safety [26]. These voltage responses contain degradation-relevant information and have therefore been used for rapid SOH estimation [27]. The difficulty is that pulse responses are also strongly SOC-dependent: even cells with similar SOH can exhibit different voltage responses at different charge states, and this SOC dependence varies with chemistry, capacity, and degradation trajectory. This is not a minor experimental detail for retired batteries. Their arrival SOC is often unknown, and exhaustive pulse measurements over many SOC levels are impractical in screening workflows [15]. As a result, SOC-related variation and SOH-related variation become coupled in the measured voltage signals [28]. Meanwhile, SOC estimation itself remains difficult for aged batteries because degradation alters voltage-response characteristics and weakens the reliability of conventional voltage look-up table approaches [29]. Joint SOC and SOH estimation from limited pulse measurements remains an unresolved practical challenge for second-life battery deployment.

To bridge this gap, we develop a machine-learning (ML)-assisted joint estimation framework for the SOC and SOH of retired battery cells using sparse voltage measurements in response to pulse current. This framework integrates short bipolar pulse excitation, feature construction, and data-efficient regression. Using pulse-response data from 270 randomly retired cells covering three chemistry types and four capacity classes, 21 voltage-based features are extracted for model development. Two ML models, i.e., extremely randomized trees (ExtraTrees) and tabular prior-data fitted network (TabPFN), are employed for joint state estimation and systematically evaluated using the diverse battery dataset. To reduce the measurement burden, eight SOC-availability cases are designed to emulate realistic measurement reduction scenarios, where missing SOC-dependent feature points are reconstructed using two interpolation methods before downstream learning. The results show that accurate SOC and SOH estimation can be achieved across heterogeneous retired cells, while near-baseline accuracy can be retained even when a substantial fraction of SOC-dependent pulse tests is removed.

Table 1
Cut-off voltages used for reference capacity calibration.

Cell chemistry	Capacity (Ah)	Discharge voltage limit (V)	Charge voltage limit (V)
NMC	2.1	2.70	4.20
NMC	21	2.70	4.20
LMO	10	2.00	4.20
LFP	35	2.50	3.65

2. Experimental setup and feature extraction

The data used in this study consist of four battery datasets, covering three major cathode chemistries and four capacity classes: 56 LFP (35 Ah), 95 LMO (10 Ah), 67 NMC (2.1 Ah), and 52 NMC (21 Ah) cells. Prior to retirement, these cells were subjected to heterogeneous operating conditions. The NMC 2.1 Ah cells were cycled under laboratory-based accelerated aging conditions, whereas the remaining cells were extracted from electric vehicles operating under three distinct usage modes. The NMC 21 Ah cells were used in pure electric configurations, while the LFP and LMO groups experienced hybrid operation profiles. Historical usage data for these cells were unavailable, which is commonly encountered in practice for retired batteries.

2.1. SOH calibration and distribution

SOH was determined at the initial stage of retirement through a reference capacity calibration. Specifically, each cell was first charged to its upper cut-off voltage (see Table 1) under a constant current of 1 C, followed by a constant-voltage phase until the current decreased to 0.05 C. The cell was subsequently discharged at 1 C to its lower cut-off voltage. The resulting discharge capacity was obtained via Coulomb counting of the current over time and taken as the available capacity of the cell. SOH was defined as the ratio of this calibrated capacity to its nominal capacity.

The SOH distributions of the four cell groups are summarized in Fig. 1. Clear differences emerge across chemistries and capacity classes. The NMC 21 Ah cells remain tightly clustered near full health (mean SOH $\mu = 0.980$, standard deviation $\sigma = 0.052$), indicating that most of these cells are still close to their beginning-of-life condition at retirement. This may occur when failure or imbalance at the pack level leads to the retirement of the entire system despite many cells remaining largely undegraded. In contrast, the LFP 35 Ah cells exhibit a moderate spread ($\mu = 0.849$, $\sigma = 0.049$), with all samples concentrated between approximately 0.75 and 1.0, suggesting varying degrees of degradation within the first-life stage. A markedly different pattern is observed for the LMO 10 Ah and NMC 2.1 Ah cells, both of which span a much wider SOH range (down to ≈ 0.5), accompanied by significantly larger variance (e.g., $\sigma = 0.115$ for LMO). These distributions indicate substantial diversity in degradation states, likely arising from differences in usage conditions, operational environments, and system-level management prior to retirement. Some cells in these groups are already close to the end of their second-life usability, while others remain relatively intact.

Overall, the dataset combines a relatively large sample size, broad SOH coverage, and diverse degradation pathways despite missing historical information. This combination, although challenging for modeling, provides a representative and practically relevant basis for studying state estimation in retired batteries.

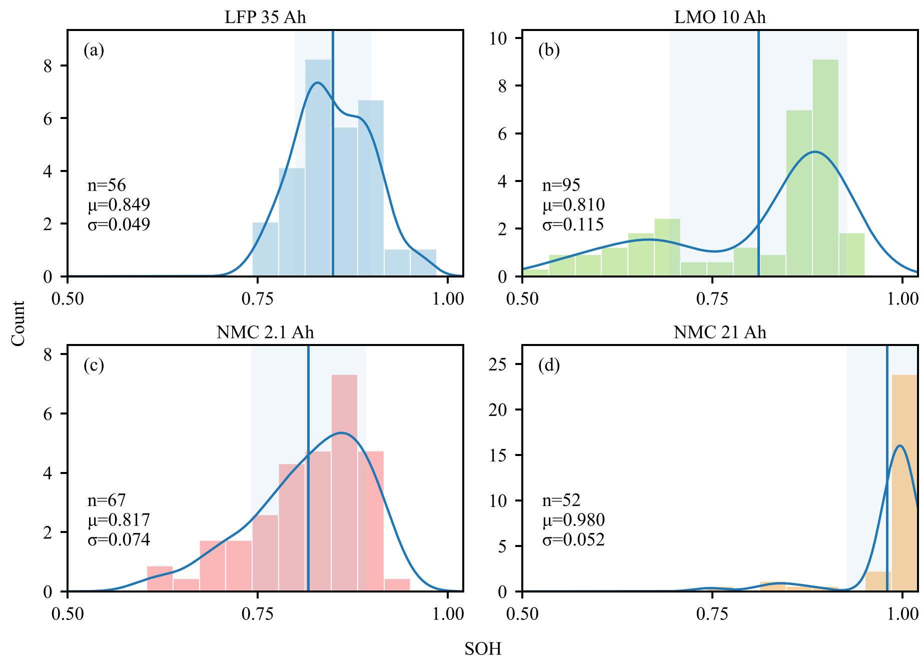

Fig. 1. SOH distributions of the four retired battery groups. The colored histograms show the empirical SOH distributions, the blue curves show the kernel density estimates, the vertical blue line denotes the mean SOH, and the shaded region represents one standard deviation around the mean. The number of cells (n), mean SOH (μ), and standard deviation (σ) are reported in each panel.

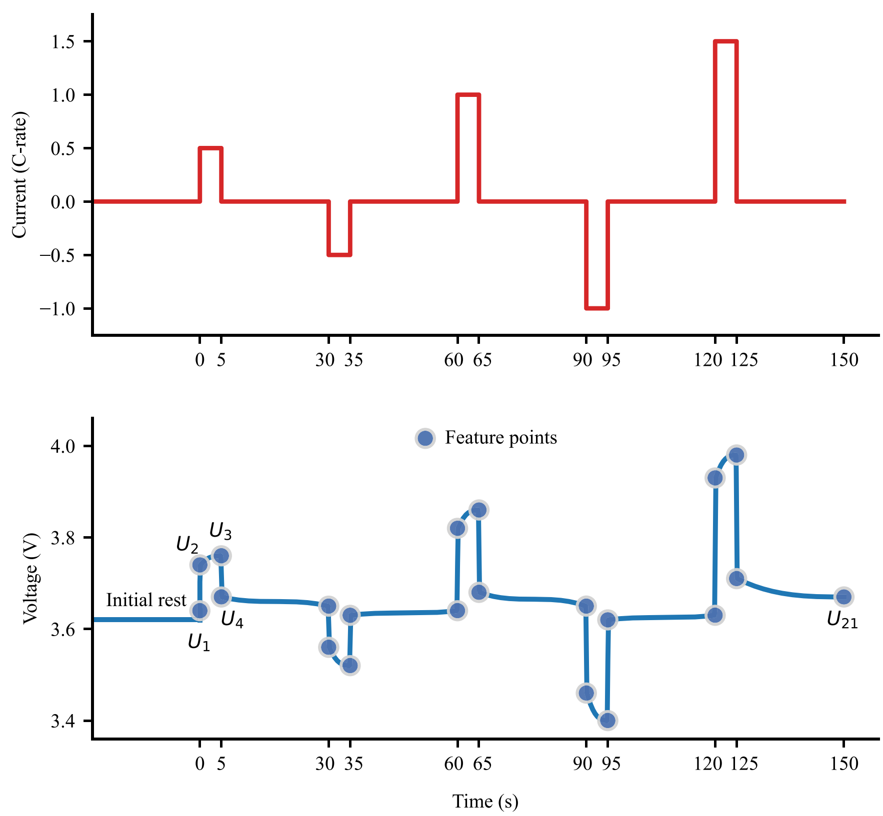

Fig. 2. Pulse current excitation and corresponding voltage response. A set of 21 characteristic feature points is extracted from the voltage trajectory at predefined sampling locations around the pulse transitions. Each pulse lasts 5 s, followed by a 25 s rest period. The measurements are recorded at 100 Hz.

2.2. Pulse tests

As discussed in Section 1, short current perturbations provide a rapid and practical means to probe battery dynamics using standard electrical measurements, making them suitable for large-scale screening of retired batteries with unknown usage histories. After capacity calibration, pulse tests were conducted over SOC levels from 5% to 50% with a uniform increment of 5%, as illustrated in Fig. 2. Such an SOC range was intentionally selected to reflect practical situations of retired lithium-ion battery cells, which are commonly maintained at low-to-medium SOC levels to minimize safety risks during storage, transport, and testing. For each target SOC, the cell SOC was adjusted from 0% by applying a 1 C constant-current charge for a prescribed duration corresponding to the desired SOC increment. In this protocol, SOC is defined with respect to the nominal capacity; therefore, each 5% SOC increment corresponds to 3 min of 1 C charging. After each adjustment step, the cell was rested for 10 min to approach a quasi-steady state before perturbation excitation. This adjustment–rest sequence was repeated sequentially across all SOC levels.

At each SOC level, a sequence of symmetric bipolar current pulses was applied to probe the voltage response while minimizing net energy transfer. Specifically, each perturbation consisted of a charge pulse followed by a discharge pulse of equal magnitude, separated by relaxation intervals. As shown in Fig. 2, the pulse duration was 5 s, followed by a 25 s relaxation period. The perturbation amplitudes were swept in ascending order as ± 0.5C, ± 1C, and ± 1.5C. This design helped maintain the assigned SOC level during testing while still exciting both charge and discharge dynamics. Voltage responses were recorded continuously during both pulse and relaxation periods, providing high-resolution dynamic information for subsequent feature extraction.

2.3. Feature extraction and visualization

Based on the voltage responses obtained from the pulse tests, 21 features, i.e., $\{U_1, U_2, \dots, U_{21}\}$, were extracted to characterize the transient voltage dynamics during both excitation and relaxation periods. As illustrated in Fig. 2, these features correspond to voltage values at predefined transition points of the pulse sequence, including the onset and termination of current excitation, as well as selected points along the relaxation trajectory that capture the temporal evolution of voltage recovery.

The extracted features at different SOC levels for four cells are shown in Fig. 3. To enable a meaningful comparison across chemistries, the selected cells have closely matched SOH values and are representative of their respective groups, which helps isolate the influence of SOC and electrochemical characteristics from that of overall degradation level.

Several observations can be made. First, even at similar SOH, the feature profiles exhibit distinct structures across chemistries and capacity classes, particularly in how they evolve with the perturbation index (see Fig. 3a). As the feature index reflects different stages of the pulse sequence and corresponding current magnitudes, the profiles reveal how the voltage responds to varying excitation intensities. Second, the SOC dependence of the features is evident within each cell type. For a given cell, feature values shift systematically with SOC, forming ordered trajectories across the SOC range. For instance, the LFP cells exhibit more clearly separated feature curves at lower SOC but increasingly clustered behavior above approximately 25% SOC, whereas the NMC 2.1 Ah cells show the opposite tendency, with denser feature curves at low SOC and progressively wider spacing at higher SOC. These patterns reflect how the voltage response evolves with charge state under a fixed electrochemical system. Third, clear differences arise across different cell types when comparing the voltage response characteristics (see Fig. 3b). The LMO cells exhibit the widest voltage range, while the LFP cells operate within a narrower voltage window. The two NMC groups share similar overall feature shapes but differ in voltage span, indicating distinct scaling of the voltage response.

These observed patterns indicate that the pulse-response features retain information related to SOC, degradation state, and electrochemical characteristics, and can thus serve as informative inputs for subsequent SOC and SOH estimation.

3. Method

SOH represents the remaining capacity and degradation level of a retired cell, and provides the basis for identifying reusable batteries, excluding severely degraded cells, and grouping cells with comparable aging states for second-life pack assembly. SOC represents the current charge state, which is often uncertain after previous use, storage, and self-discharge. It is therefore essential to estimate SOH and SOC for large-scale second-life battery applications. While the SOH and SOC information was carefully calibrated in Sections 2.1 and 2.2, these labels are time-consuming and energy-intensive to obtain, and are used here only as reference values for the training and evaluation of ML models. Our objective is to estimate these two states for each battery cell from minimal experimental data while maintaining high accuracy and robustness.

Conventional data-driven models for battery diagnosis generally require sufficiently dense and well-distributed measurements [30–32]. Such models may fail when applied to retired battery cells with sparse and irregular measurements. To address this limitation, we develop a three-step framework that integrates diagnostic pulse-testing protocols, synthetic data generation, and ML models.

3.1. Reduced experiments under different testing scenarios

While the considered SOC range is $[5\%, 50\%]$, performing experiments at each specified SOC level requires an adjustment–rest process (see Section 2.2). This procedure is time- and resource-intensive, particularly when a large number of heterogeneous retired cells must be screened. Reducing the number of required SOC calibration points would therefore enable faster second-life battery screening and more efficient reuse/recycling decisions. To systematically evaluate how the number and distribution of available pulse measurements affect feature reconstruction and subsequent model performance, we construct eight testing cases, as illustrated in Fig. 4. These cases emulate representative measurement conditions encountered in practice, including alternating availability, varying degrees of sparsity, continuous gaps in SOC coverage, and regionally biased SOC coverage across the SOC range. For example, in Case 4, pulse tests are conducted only at 5%, 25%, and 50% SOC.

3.2. Synthetic data generation by interpolation

Reducing the number of SOC-dependent experiments inevitably limits the amount of available training data, which can degrade the performance of data-driven models. More importantly, it results in incomplete coverage of the SOC-dependent feature space, hindering the model's ability to learn the underlying feature–target relationships. To address this, we reformulate the problem as the reconstruction of SOC-dependent feature trajectories from incomplete observations and employ interpolation to approximate the underlying structure. Specifically, two interpolation methods are used to reconstruct pulse-response features at unmeasured SOC levels within the observed range, thereby enriching the training set without additional experiments.

Linear interpolation. Based on the smooth variation of each voltage feature with SOC (see Fig. 3), linear interpolation is applied. Missing voltage features at unmeasured SOC levels are estimated using straight-line connections between adjacent measured SOC points, which is equivalent to a distance-weighted average of the two neighboring points. Specifically, for a missing SOC level s between two measured SOC levels s_ℓ and $s_{\ell+1}$, the interpolated value of the j-th voltage feature is given by

$$\tilde{U}_j(s) = U_j(s_\ell) + \frac{s - s_\ell}{s_{\ell+1} - s_\ell}\left[U_j(s_{\ell+1}) - U_j(s_\ell)\right], \quad \text{for } s_\ell < s < s_{\ell+1}, \tag{1}$$

where $j \in \{1, \dots, 21\}$, and $U_j(s_\ell)$, $U_j(s_{\ell+1})$ are the corresponding voltage measurements. The interpolation is performed independently for each feature across the SOC range.

PCHIP method. To better capture local curvature and nonlinearity, the piecewise cubic Hermite interpolating polynomial (PCHIP) method is also employed [33]. A shape-preserving piecewise cubic function is fitted over the measured SOC points to reconstruct the SOC-dependent voltage-feature trajectories. Compared with linear interpolation, PCHIP

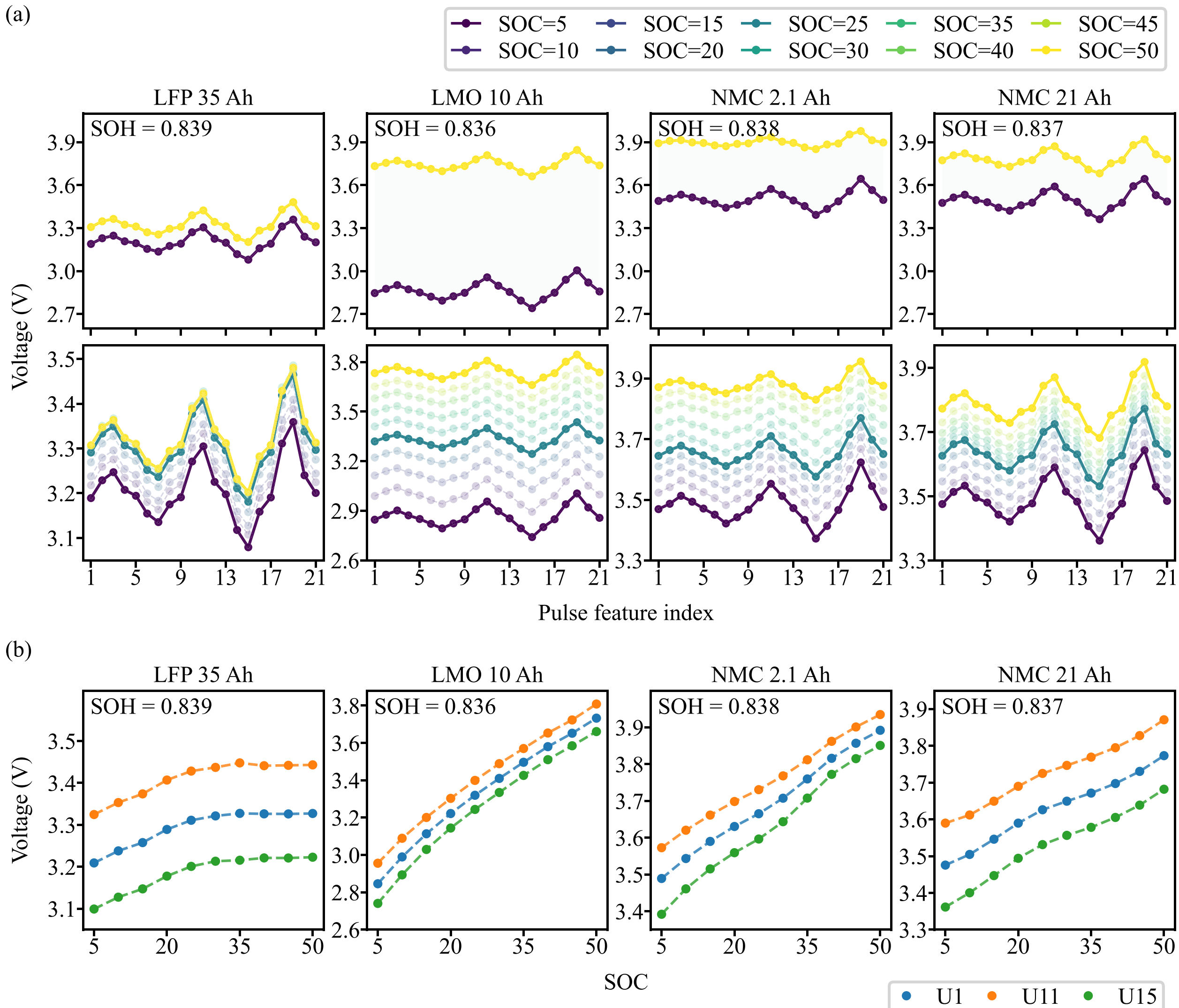

Fig. 3. Voltage-response features extracted from pulse tests for representative retired cells with comparable SOH across four battery groups (LFP 35 Ah, LMO 10 Ah, NMC 2.1 Ah, and NMC 21 Ah). (a) Feature profiles as a function of pulse feature index at different SOC levels. (b) SOC-dependent evolution of selected features (U_1, U_{11}, and U_{15}), showing smooth variation across the SOC range and chemistry-dependent characteristics.

incorporates local slope information estimated from neighboring intervals, enabling a smoother representation while preserving monotonicity. For the j-th voltage feature, the interpolated value $\tilde{U}_j(s)$ over the SOC interval $[s_\ell, s_{\ell+1}]$ is expressed as

$$\tilde{U}_j(s) = h_0(t)U_j(s_\ell) + h_1(t)(s_{\ell+1} - s_\ell)d_{j,\ell} + h_2(t)U_j(s_{\ell+1}) + h_3(t)(s_{\ell+1} - s_\ell)d_{j,\ell+1}, \tag{2}$$

where $d_{j,\ell}$ and $d_{j,\ell+1}$ denote the PCHIP slopes separately estimated at s_ℓ and $s_{\ell+1}$, $t = (s - s_\ell)/(s_{\ell+1} - s_\ell)$, and the cubic Hermite basis functions are

$$h_0(t) = 2t^3 - 3t^2 + 1, \quad h_1(t) = t^3 - 2t^2 + t, \tag{3}$$

$$h_2(t) = -2t^3 + 3t^2, \qquad h_3(t) = t^3 - t^2. \tag{4}$$

3.3. Regression models for SOH and SOC estimation

Based on the reconstructed SOC-dependent feature set, each pulse-test sample is represented by a feature vector $\mathbf{x}_i = [U_1, U_2, \ldots, U_{21}]_i \in \mathbb{R}^{21}$, where i indexes the battery cell. The corresponding targets are SOH and SOC. The estimation problem is formulated within a supervised nonlinear regression framework. In this study, SOH and SOC are modeled using separate regression functions, i.e., $\hat{y}_i^{\mathrm{SOH}} = f_{\mathrm{SOH}}(\mathbf{x}_i)$ and $\hat{y}_i^{\mathrm{SOC}} = f_{\mathrm{SOC}}(\mathbf{x}_i)$, following independent training and model selection procedures. Given the limited and irregular SOC-dependent measurements in second-life scenarios, emphasis is placed on data-efficient models that can generalize under sparse and partially reconstructed feature inputs. To this end, two representative regression approaches, namely the extremely randomized trees (ExtraTrees) regressor and the tabular prior-data fitted network (TabPFN) are employed.

ExtraTrees model: ExtraTrees is adopted as a baseline regressor due to its robustness in handling high-dimensional tabular data with limited sample size [34]. In the present problem, the input features consist of pulse-response voltages measured at different temporal points within a short excitation sequence, which exhibit strong correlations and moderate noise arising from measurement and operational variability. By introducing randomization in both feature selection and split thresholds, ExtraTrees reduces the risk of overfitting to such local variations and measurement noise [35]. This property is particularly relevant for the employed battery dataset, where the number of available cells is limited and the feature–target relationships vary across chemistries

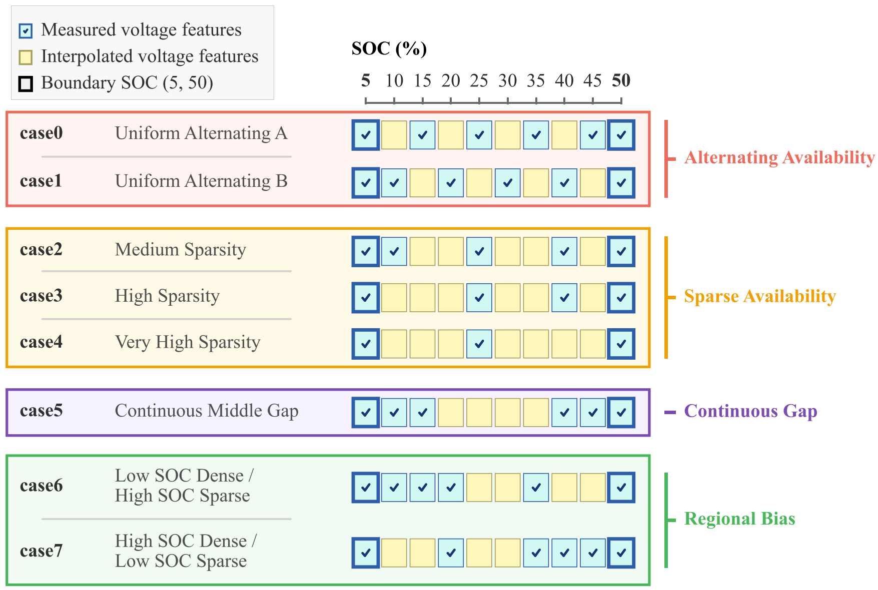

Fig. 4. Overview of the eight SOC measurement configurations considered in this study. Check-marked cells indicate measured pulse voltage features, while blank cells indicate SOC levels at which the pulse voltage features are reconstructed by interpolation. The configurations cover alternating measurements, varying levels of sparsity, a continuous middle-SOC gap, and regionally biased SOC coverage. Boundary SOC points at 5% and 50% are always retained.

and degradation states. As a result, ExtraTrees provides a stable and interpretable baseline for evaluating the effectiveness of the proposed pulse-based estimation framework.

TabPFN model: TabPFN is employed as a data-efficient foundation model for tabular regression [36]. Unlike conventional models that require task-specific parameter training, TabPFN is pre-trained on a large collection of synthetic tabular prediction tasks and performs inference on a new dataset through in-context learning. In the present implementation, for each target $q \in \{\mathrm{SOH}, \mathrm{SOC}\}$, the prediction can be written as

$$\hat{y}_*^{(q)} = f_\theta^{\mathrm{TabPFN}}\left(\mathbf{x}_* \,\middle|\, \mathcal{D}_{\mathrm{train}}^{(q)}\right), \tag{5}$$

where x_* is the pulse-feature vector of a test sample, $\mathcal{D}_{train}^{(q)}$ denotes the observed training samples for the corresponding target variable q, and θ represents the fixed parameters of the pre-trained TabPFN model. In this setting, the training samples are used as contextual examples rather than to update the model weights.

This design is well aligned with the battery problem, where only limited samples are available and the feature–target relationships must be inferred from sparse and partially reconstructed SOC-dependent data. By leveraging a pre-trained prior over diverse tabular structures and conditioning on the observed battery samples, TabPFN can infer feature–target relationships directly at inference time. This reduces the need for extensive hyperparameter tuning. To the best of our knowledge, this is the first application of TabPFN to pulse-based SOH and SOC estimation in battery systems. Under the same SOC-availability scenarios, interpolation settings, and train–test splits as the ExtraTrees baseline, TabPFN provides a complementary data-driven approach for evaluating estimation performance.

4. Results and discussion

Model performance is evaluated using Monte Carlo cross-validation to reduce the influence of sample-specific bias and data partitioning variability. For each battery group, 80% of the cells are randomly selected for training, while the remaining 20% are reserved for testing. This random splitting is repeated 10 times, and all reported results correspond to the average over these independent realizations. This procedure provides a stable estimate of predictive performance under limited and heterogeneous data conditions.

Two evaluation metrics are adopted to evaluate model accuracy, namely the mean absolute error (MAE) and the mean absolute percentage error (MAPE), defined as

$$\mathrm{MAE} = \frac{1}{N}\sum_{i=1}^{N} \left| y_i - \hat{y}_i \right|, \tag{6}$$

$$\mathrm{MAPE} = \frac{1}{N}\sum_{i=1}^{N} \left| \frac{y_i - \hat{y}_i}{y_i} \right| \times 100\%, \tag{7}$$

where N denotes the number of samples in the test set, and y_i and $\hat{y}_i$ represent the reference and estimated values of the target variable (SOH or SOC), respectively. These two metrics serve complementary roles. MAE quantifies the absolute deviation in the estimation tasks, where the targets (SOH and SOC) have direct physical interpretations. MAPE, by normalizing the error with respect to the reference magnitude, is used to evaluate the interpolation accuracy of SOC-dependent features across different scales. This distinction is necessary because the reconstructed feature trajectories act as intermediate inputs to the downstream learning models, and inaccuracies introduced at this stage may propagate in a non-uniform manner to the final SOH and SOC estimations.

In real-world battery screening, decisions are typically made based on thresholding rules rather than continuous estimates. In particular, SOH levels of 0.75–0.8 are commonly used to distinguish batteries suitable for continued first-life use from those to be redirected to second-life applications or recycling. Under this setting, a critical requirement is to reliably identify cells that remain in the high-SOH region. Although the models are trained to produce continuous SOH estimates, we further threshold the predicted SOH values at 0.8 to evaluate decision-oriented screening performance. The recall of the SOH $\geq$ 0.8 class is defined as

$$\mathrm{Recall}_{\mathrm{SOH}} = \frac{N_{\mathrm{TP}}}{N_{\mathrm{TP}} + N_{\mathrm{FN}}}, \tag{8}$$

where N_{TP} denotes the number of cells with true SOH $\geq$ 0.8 that are correctly estimated as such during testing, and N_{FN} denotes the number of cells with true SOH $\geq$ 0.8 that are incorrectly classified below the threshold.

Table 2
Dataset-specific hyperparameter settings of the ExtraTrees regressor for SOH and SOC estimation. Here, n_{est} denotes the number of trees, n_{split} the minimum number of samples required to split an internal node, n_{leaf} the minimum number of samples required at a leaf node, and m_{feat} the number of candidate features considered when searching for the best split.

Target	Dataset	n_{est}	n_{split}	n_{leaf}	m_{feat}
SOH	LFP 35 Ah	1000	2	4	5
	LMO 10 Ah	300	2	2	–
	NMC 2.1 Ah	1000	2	1	–
	NMC 21 Ah	1000	2	1	–
SOC	LFP 35 Ah	300	2	1	–
	LMO 10 Ah	1000	2	1	–
	NMC 2.1 Ah	1000	2	1	–
	NMC 21 Ah	500	2	2	–

4.1. Results of SOH estimation

The SOH estimation results are obtained using the ML models developed in Section 3.3. In this baseline evaluation, pulse features from the entire tested SOC range, namely 5–50% SOC, are used as model inputs. Therefore, this part does not involve the testing scenarios or interpolation methods described in Sections 3.1 and 3.2. TabPFN is applied without hyperparameter tuning, while ExtraTrees is used with the cell-specific hyperparameter settings given in Table 2. The results are discussed for two cases: the full testing set and the practically important high-SOH subset with SOH ≥ 0.8.

According to Fig. 5(a)–(d), both ExtraTrees and TabPFN achieve consistent SOH estimation across the four battery types, with TabPFN yielding lower MAE in all cases. For the full testing set, the MAE values of TabPFN are 0.0306, 0.0223, 0.0256, and 0.0076 for LFP 35 Ah, LMO 10 Ah, NMC 2.1 Ah, and NMC 21 Ah cells, respectively. For reference, reported SOH estimation errors in the literature typically fall in the range of 0.03–0.05 when large-scale real-world datasets are available, and can drop below 0.01 under controlled laboratory conditions with dense measurements [30,37]. In contrast, the setting considered here is substantially more constrained: each cell is characterized only by sparse pulse-test data obtained within a short excitation window, without any historical usage information or aging trajectory. Despite these limitations, the achieved error levels are comparable to those reported for data-rich scenarios, particularly for the LMO and NMC datasets. This indicates that reliable SOH screening can be achieved without relying on historical data or long-duration testing. As will be further shown in Section 4.4, the proposed method also provides a clear improvement over existing pulse-based approaches under the same data constraints.

The estimation accuracy varies markedly across the cell types. For both models, the best performance is observed for the NMC 21 Ah cells, with MAE values significantly lower than those of the other three cell types. This difference should not be attributed to the models alone. As shown in Fig. 1, all NMC 21 Ah samples lie within the SOH ≥ 0.75 region, with most concentrated near fresh-cell conditions. Such a narrow distribution leads to a more regular feature–target relationship, which simplifies the regression task. The high accuracy achieved for this dataset should therefore be interpreted in light of its SOH distribution,

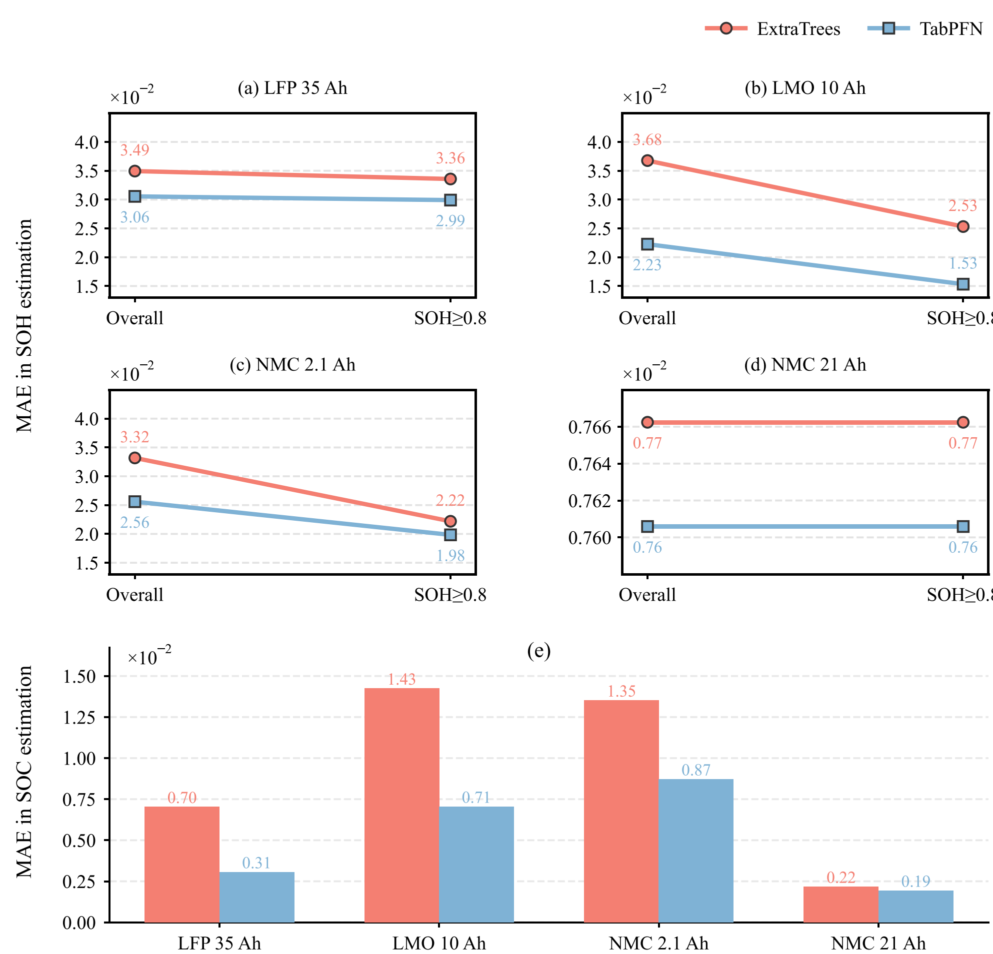

Fig. 5. Comparison of the estimation performance of ExtraTrees and TabPFN across the four cell datasets. In this baseline evaluation, pulse features from the entire tested SOC range are used for training.

Table 3
Proportion of training samples with SOH ≥ 0.8 and classification recall for testing samples with SOH ≥ 0.8.

Battery Type	Model	Proportion of train cells with SOH ≥ 0.8 (%)	Recall for SOH ≥ 0.8
LFP 35 Ah	ExtraTrees	83.4	0.997
	TabPFN	83.4	0.944
LMO 10 Ah	ExtraTrees	68.7	0.926
	TabPFN	68.7	0.987
NMC 2.1 Ah	ExtraTrees	64.2	0.901
	TabPFN	64.2	0.904
NMC 21 Ah	ExtraTrees	97.6	0.988
	TabPFN	97.6	0.973

rather than as evidence that large-format NMC cells are intrinsically easier to estimate. The same trend becomes more evident when the evaluation is restricted to cells with SOH ≥ 0.8. In this high-SOH subset, the MAE is generally lower than that of the full testing set. The reduction is particularly clear for LMO 10 Ah cells under TabPFN, where the MAE decreases by 39.5%. Therefore, when the evaluation is confined to a narrower SOH region, the mapping from pulse-response features to SOH becomes less dispersed, and the regression task becomes better conditioned.

The high-SOH subset is also important from a screening perspective. As listed in Table 3, the proportion of training samples with SOH ≥ 0.8 varies considerably across the four datasets, ranging from 64.2% for NMC 2.1 Ah cells to 97.6% for NMC 21 Ah cells. The recall values for the SOH ≥ 0.8 class are consistently above 0.90 for both models, indicating that most cells truly belonging to the high-SOH region are correctly retained above the threshold. The highest recall is obtained by ExtraTrees for LFP 35 Ah cells, reaching 0.997, and by TabPFN for LMO 10 Ah cells, reaching 0.987. Notably, the recall performance shows a clear dependence on the underlying data distribution: datasets with a higher proportion of high-SOH training samples generally lead to more reliable identification of this region. These results indicate that the pulse-feature-based framework is not only able to reduce continuous SOH estimation error, but also supports screening decisions that avoid prematurely assigning still-healthy cells to second-life use or recycling.

4.2. Results of SOC estimation

Using the same data splitting strategy as in the SOH task and the model settings in Table 2, the SOC estimation results are reported in Fig. 5(e). The first observation is that the proposed estimation framework provides accurate SOC estimation across all four cell groups. Even with the baseline ExtraTrees regressor, the MAE remains below 0.0143 for all datasets. This confirms that the designed short-pulse profile and the extracted voltage-response features contain sufficient SOC-relevant information for regression. The result is particularly meaningful for LFP cells, where conventional voltage-based SOC estimation is often difficult because of the plateau in the open-circuit voltage (OCV) profile [38,39]. Here, the input contains both the initial voltage level and the subsequent pulse-response features, which encode additional dynamic information related to resistance, relaxation and local electrochemical response, thereby reducing the ambiguity in SOC estimation.

On top of this general effectiveness, TabPFN consistently improves upon ExtraTrees across the four datasets. Its MAE values are 0.0031, 0.0071, 0.0087, and 0.0019 for LFP 35 Ah, LMO 10 Ah, NMC 2.1 Ah, and NMC 21 Ah cells, respectively (see the light blue bars in Fig. 5e). The improvement is especially clear for the LMO 10 Ah and NMC 2.1 Ah datasets, where TabPFN reduces the SOC estimation error by more than half. This trend is consistent with the SOH estimation results in Section 4.1, suggesting that TabPFN is more effective at extracting stable feature–target mappings from limited and heterogeneous tabular battery data.

Dataset-dependent differences are still visible. The NMC 21 Ah cells give the lowest SOC estimation error for both regressors, with MAE values of 0.0019 for TabPFN and 0.0022 for ExtraTrees. This is consistent with Fig. 3, where the NMC 21 Ah pulse features exhibit relatively smooth and regular variations with SOC. By contrast, the LMO 10 Ah and NMC 2.1 Ah datasets show larger feature variations across SOC, especially in the representative pulse-feature trajectories, and correspondingly lead to higher estimation errors. These observations indicate that the accuracy of pulse-feature-based SOC estimation is governed not only by the regression model, but also by how regularly the pulse-response features evolve with SOC for a given cell group.

4.3. Results of interpolation methods

To assess the effectiveness of the experiment reduction and synthetic data generation introduced in Section 3, interpolation errors are evaluated under the eight SOC-availability cases across the four battery datasets. As shown in Fig. 6(a), both interpolation methods consistently yield low errors. The feature-wise error distributions in Fig. 6(b) further confirm that the interpolation accuracy is consistently maintained across the 21 extracted features. PCHIP generally outperforms linear interpolation across all datasets and SOC-availability cases, with average MAPE values remaining below 0.60% for linear interpolation and below 0.39% for PCHIP. These results demonstrate that the selected interpolation methods provide an effective means for reconstructing SOC-dependent pulse-response features.

Consistent with the state estimation results, clear dataset-dependent differences are observed. The NMC 2.1 Ah cells exhibit the lowest interpolation errors, with average MAPE values below 0.22% for linear interpolation and below 0.20% for PCHIP. This can be attributed to the relatively smooth and monotonic variation of pulse-response features with SOC (see Fig. 3). In contrast, the advantage of PCHIP becomes more evident for the LMO cells, where local nonlinear variations in the feature–SOC relationship are more pronounced, leading to consistently lower errors compared with linear interpolation.

The interpolation accuracy also depends on the SOC-availability pattern. In general, the two uniform alternating cases (Cases 0–1) result in the lowest interpolation errors across all datasets, as the retained SOC points are evenly distributed over the full SOC range and provide balanced local support. By contrast, higher errors are observed when the measurements are further reduced or unevenly distributed. In particular, Case 4 suffers from insufficient local support due to very sparse measurements, while Case 5 introduces a continuous gap that degrades interpolation accuracy around the missing region. The impact of these interpolation errors on downstream state estimation is examined in the next subsection.

4.4. SOH and SOC estimation under reduced SOC-dependent measurements

To examine how the number and distribution of available pulse measurements influence SOH and SOC learning, we extend the analysis in Section 4.3 from interpolation accuracy to learning performance. For each of the eight SOC-availability cases (see Fig. 4), three training settings are considered: no interpolation, linear interpolation, and PCHIP. The no-interpolation setting uses only the measured pulse responses, whereas the interpolation-based settings augment the training set by reconstructing missing responses at unmeasured SOC levels. All results are compared with the full-measurement baselines established in Sections 4.1 and 4.2.

SOH estimation. For SOH estimation, interpolation-based training consistently improves the results compared with the no-interpolation setting (Fig. 7 and Table 4). Across all cell groups, the estimation error increases as the number of SOC-dependent pulse tests decreases. When six SOC levels are available (Cases 0–1 and 5–7), the performance differences among these cases are small, and the best-performing configurations remain close to the full-measurement baselines, with absolute MAE differences ranging from 0.0001 to 0.0018 across the four cell

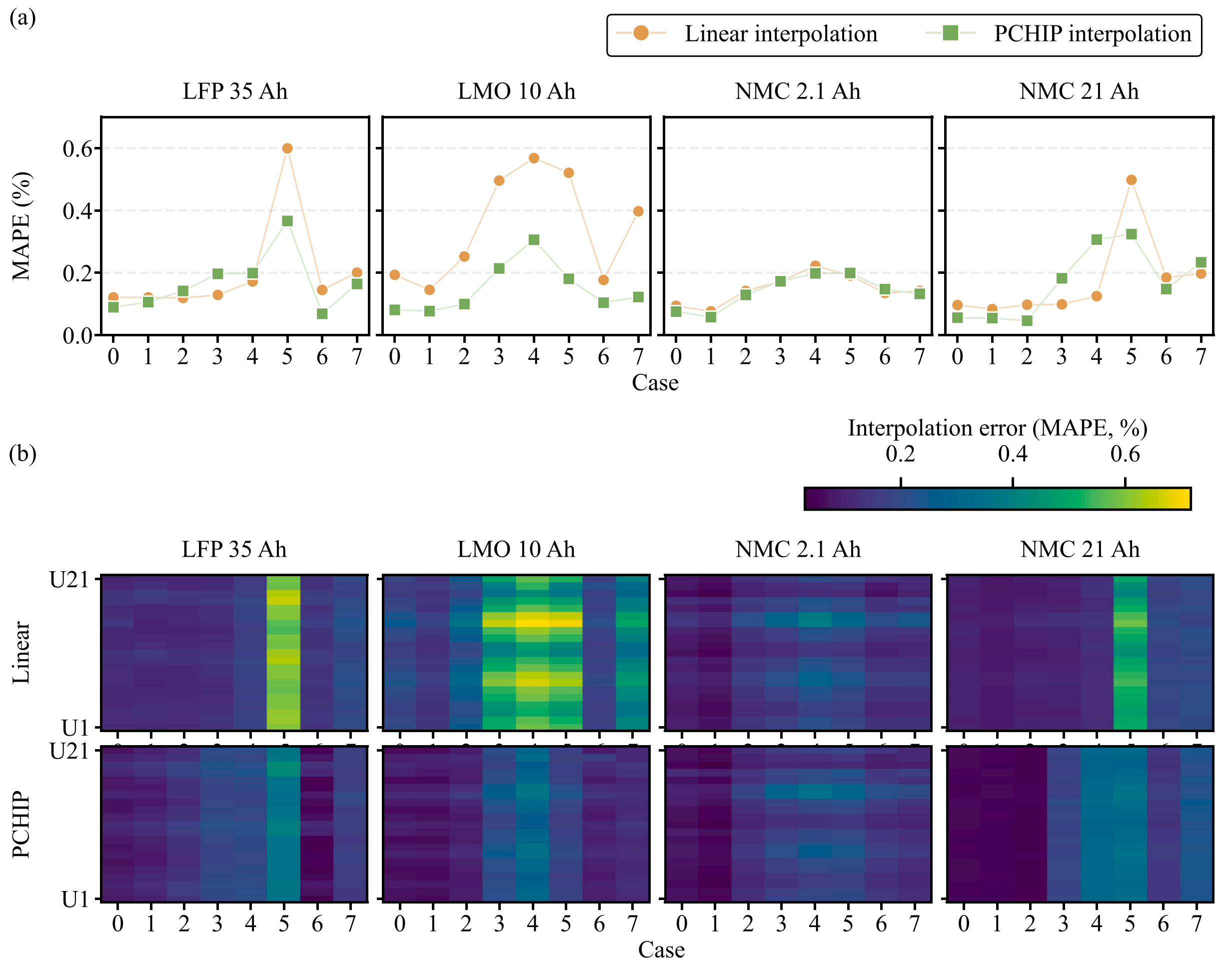

Fig. 6. Interpolation error comparison under the eight SOC-availability cases. (a) Case-wise average error. (b) Feature-wise error heatmaps.

groups. However, the optimal SOC-availability pattern depends on the cell group. For the LFP, NMC 2.1 Ah, and NMC 21 Ah datasets, alternating SOC coverage (Cases 0–1) yields better performance, consistent with the more uniform support provided across the SOC range. In contrast, the LMO dataset achieves its best result in Case 5, where the middle SOC region is absent. This behavior suggests that, for this dataset, the feature distributions in the retained low- and high-SOC regions remain sufficiently consistent to allow accurate reconstruction of the missing intermediate region without introducing significant mismatch.

These results indicate that the loss of SOC-dependent measurements does not translate proportionally into SOH estimation degradation. Even when the number of pulse tests is reduced by 40% (i.e., from ten to six SOC levels), the estimation error is only marginally higher than the full-measurement baseline, with the maximum MAE reaching 0.031 across all cell groups (see Table 4). This level of SOH estimation accuracy is notably competitive under the considered setting of randomly retired cells without any historical information. For comparison, recent pulse-based SOH estimation approaches under similar conditions typically report errors around 0.06, even when assisted by advanced data augmentation or generative learning strategies [40]. The present framework therefore reduces the estimation error by approximately 48%.

SOC estimation. The impact of interpolation on SOC estimation is also evident (see Table 5 and Fig. 8). For the studied cell groups, TabPFN under the best-performing cases achieves accuracy close to the corresponding full-measurement baselines, with absolute MAE differences of at most 0.0104. However, the performance differs significantly across cell groups. For the LMO cells, the interpolation-based result is even slightly better than the baseline, likely due to variations from repeated random splits. As the number of available SOC measurements decreases, the sensitivity to reduced SOC coverage is more pronounced than that observed in SOH estimation. Among the four cell groups, LMO maintains near-baseline accuracy under sparse SOC conditions, whereas LFP, NMC 2.1 Ah, and NMC 21 Ah exhibit noticeable performance deterioration. Overall, even when up to 70% of the SOC-dependent measurements are removed (Case 4), the SOC estimation error remains below 1.8%.

Correlation analyses. The influence of interpolation on downstream estimation can be further examined through the correlation between interpolation error and the corresponding increase in estimation error, defined as the deviation from the baseline (light bars in Figs. 7 and 8). As shown in Fig. 9, the correlation coefficients vary substantially across tasks and cases, reflecting the different roles of interpolation in SOH and SOC estimation.

For SOH estimation, interpolation errors are not directly mapped to target errors, leading to a complex and nonlinear relationship between them. From a practical perspective, the estimation performance is not merely a consequence of interpolation accuracy, but reflects a structural property of the problem: SOH is a cell-level invariant during the test process, and the SOC-dependent pulse responses provide redundant yet complementary observations of the same underlying degradation state. As a result, once a minimum SOC coverage is retained, the learning model can still recover a stable feature–target mapping, even under partially observed conditions.

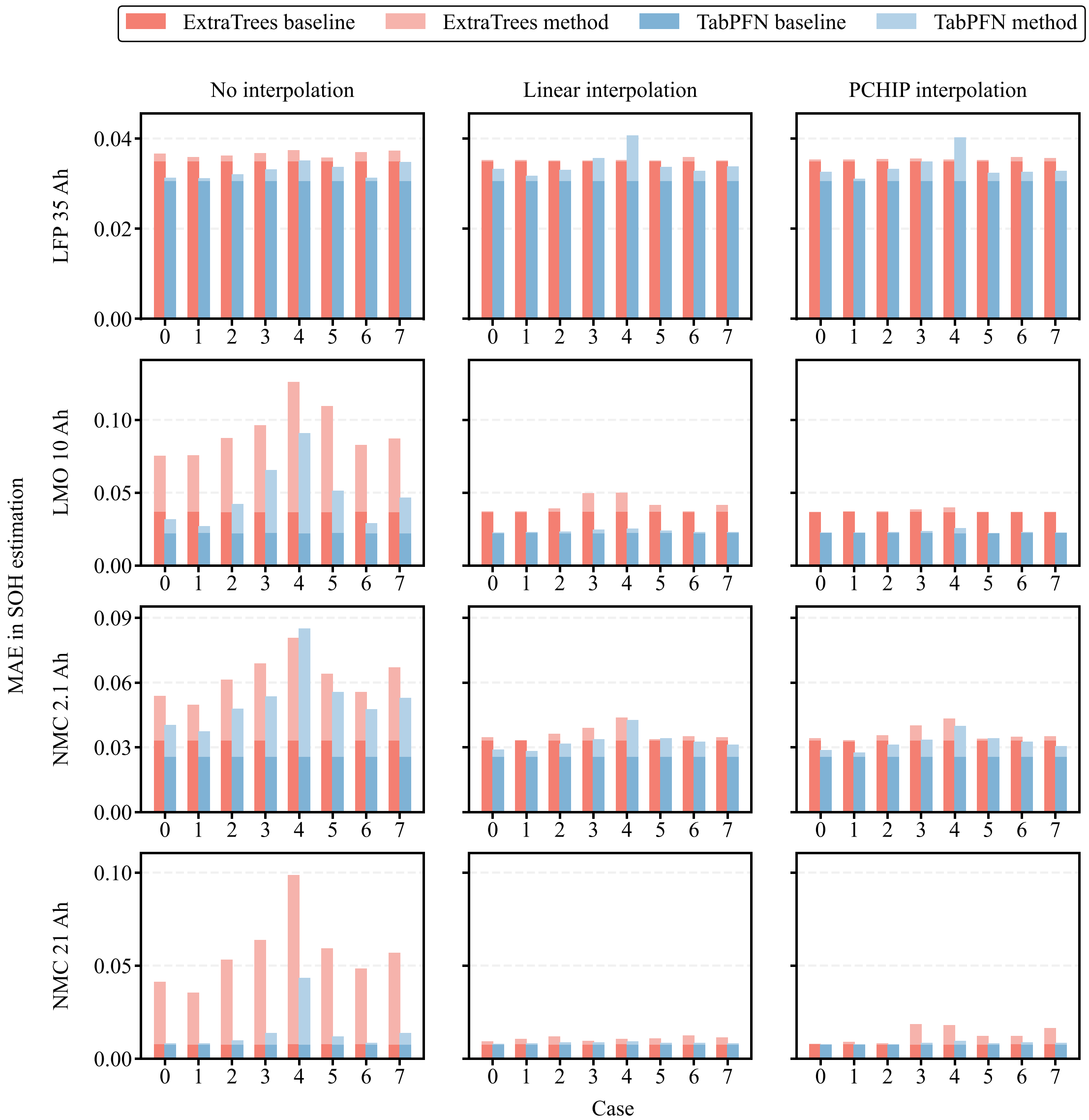

Fig. 7. SOH estimation performance when SOC-dependent measurements are reduced during training. Baseline models (dark bars) correspond to models trained using pulse features across all SOC levels (5%–50%), whereas the proposed method results are represented by light bars. All bars represent absolute MAE values. The difference between each light bar and its corresponding dark bar indicates the deviation from the baseline under no interpolation, linear interpolation, or PCHIP settings.

Table 4
SOH estimation error (MAE) of TabPFN under different SOC-availability cases. Values are reported as the mean ± standard deviation over ten Monte Carlo train–test splits. Across the three settings (no interpolation, linear interpolation, and PCHIP), the best result is reported, predominantly achieved by PCHIP. "6 SOC" refers to the cases where six out of the ten SOC levels are retained, corresponding to cases 0–1 and 5–7.

Cell group	6 SOC (Best case)	5 SOC (Case 2)	4 SOC (Case 3)	3 SOC (Case 4)	Baseline
LFP 35 Ah	0.0310 ± 0.0048 (Case 1)	0.0330 ± 0.0046	0.0348 ± 0.0041	0.0402 ± 0.0038	0.0306 ± 0.0052
LMO 10 Ah	0.0222 ± 0.0041 (Case 5)	0.0229 ± 0.0043	0.0235 ± 0.0038	0.0251 ± 0.0042	0.0223 ± 0.0046
NMC 2.1 Ah	0.0274 ± 0.0034 (Case 1)	0.0312 ± 0.0033	0.0334 ± 0.0025	0.0399 ± 0.0038	0.0256 ± 0.0028
NMC 21 Ah	0.0077 ± 0.0028 (Case 0)	0.0076 ± 0.0024	0.0086 ± 0.0031	0.0093 ± 0.0032	0.0076 ± 0.0027

In contrast, for SOC estimation, interpolation reconstructs missing feature–target pairs at unmeasured SOC levels, and errors in the reconstructed pulse features are directly associated with SOC labels, thereby introducing inaccuracies into the training data. As a result, the correlation between interpolation error and estimation error is generally stronger than in SOH estimation, although it is not strictly one-to-one at the case level. In several cases, higher interpolation error still leads to lower estimation error, while lower interpolation error does not necessarily yield better performance. This can be partly explained by the fact that interpolation error is averaged over all 21 features, whereas the estimation model may rely more heavily on a subset of SOC-sensitive features. Consequently, a lower average interpolation error does not necessarily imply more accurate reconstruction of the most informative features. In addition, differences in the retained SOC regions across cases

Table 5
SOC estimation error (MAE) of TabPFN under different SOC-availability cases. Values are reported as the mean ± standard deviation over ten Monte Carlo train–test splits. The best result is reported across the three interpolation settings, which is predominantly achieved by PCHIP. "6 SOC" refers to the cases where six out of the ten SOC levels are retained, corresponding to cases 0–1 and 5–7.

Cell group	6 SOC (Best case)	5 SOC (Case 2)	4 SOC (Case 3)	3 SOC (Case 4)	Baseline
LFP 35 Ah	0.0036 ± 0.0010 (Case 0)	0.0100 ± 0.0010	0.0112 ± 0.0009	0.0135 ± 0.0009	0.0031 ± 0.0010
LMO 10 Ah	0.0067 ± 0.0024 (Case 5)	0.0071 ± 0.0026	0.0075 ± 0.0024	0.0086 ± 0.0024	0.0071 ± 0.0029
NMC 2.1 Ah	0.0097 ± 0.0009 (Case 0)	0.0117 ± 0.0012	0.0134 ± 0.0011	0.0178 ± 0.0012	0.0087 ± 0.0010
NMC 21 Ah	0.0021 ± 0.0018 (Case 0)	0.0019 ± 0.0015	0.0025 ± 0.0017	0.0046 ± 0.0022	0.0019 ± 0.0017

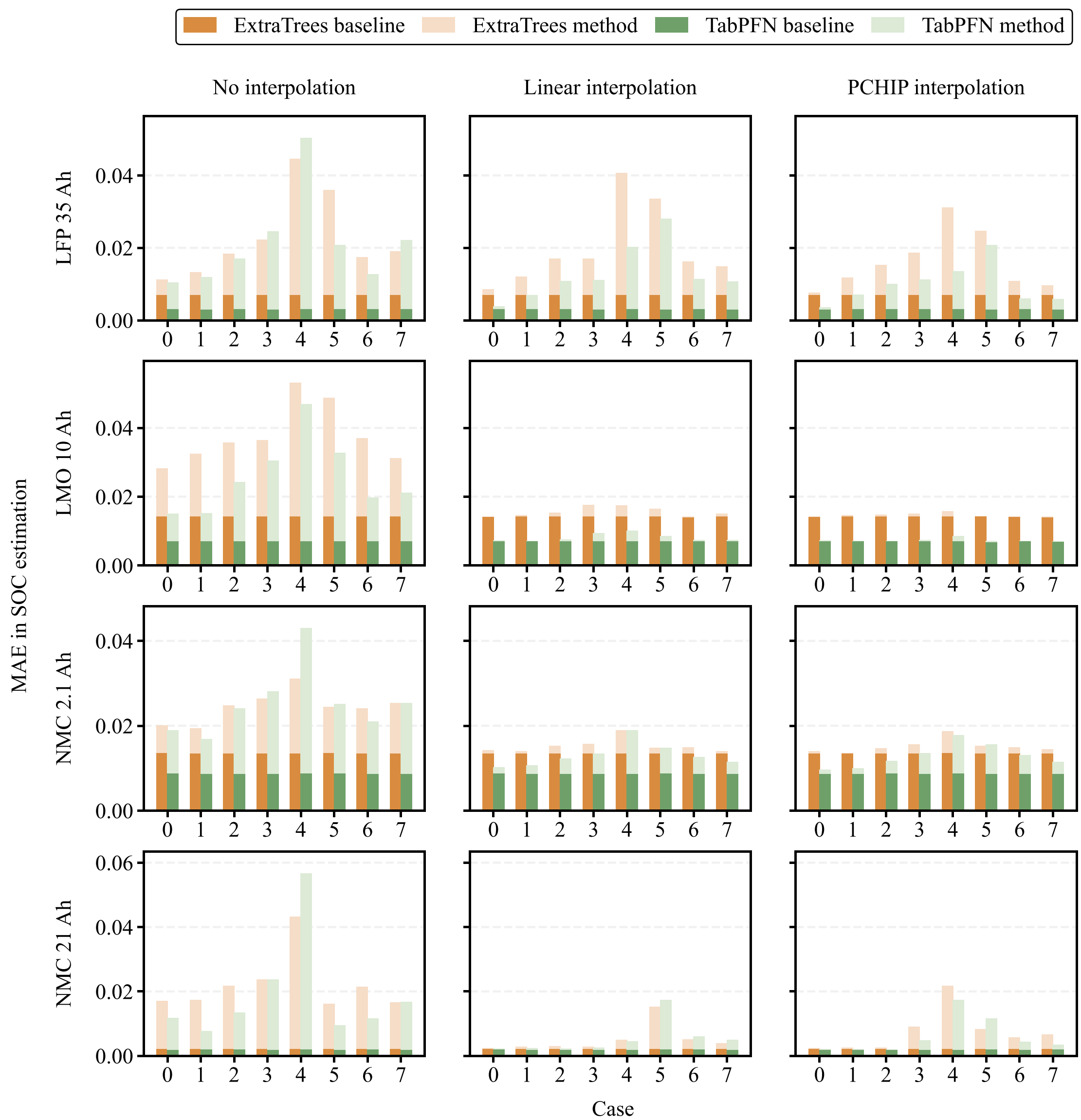

Fig. 8. SOC estimation performance when SOC-dependent measurements are reduced during training. Baseline models (dark bars) correspond to models trained using pulse features across all SOC levels (5%–50%), whereas the proposed method results are represented by light bars. All bars represent absolute MAE values. The difference between each light bar and its corresponding dark bar indicates the deviation from the baseline under no interpolation, linear interpolation, or PCHIP settings.

further influence how effectively the model learns the feature–target relationship.

Summary. These results reveal a clear asymmetry between the two estimation tasks under reduced SOC-dependent measurements. While SOH estimation remains robust to measurement sparsity due to its invariant nature, SOC estimation is more sensitive to the coverage and distribution of available measurements, reflecting its inherently local dependence on SOC-specific features.

4.5. Applicability of the proposed framework and beyond

Despite the promising estimation performance, the applicability of the proposed framework should be interpreted within the scope of the

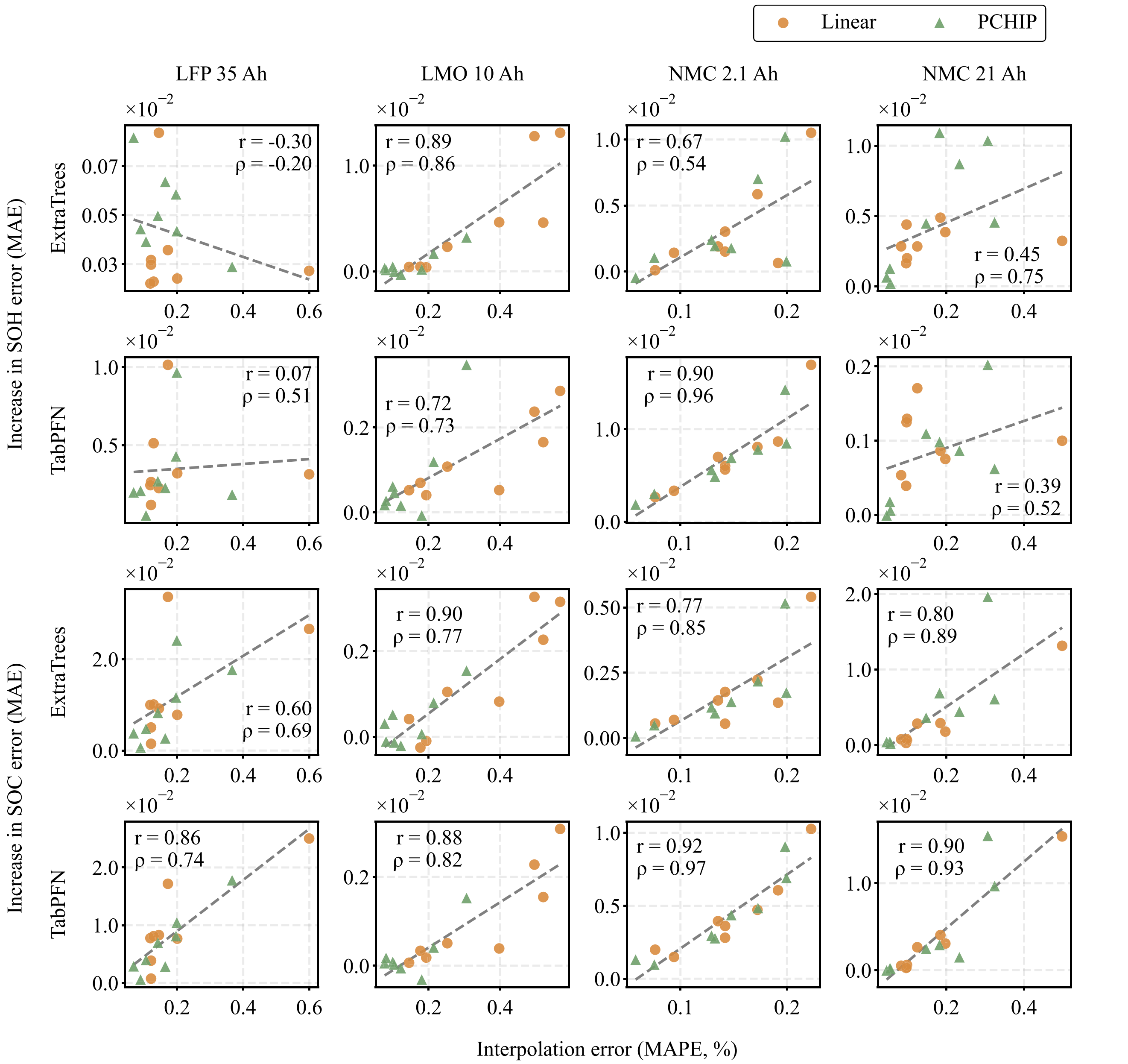

Fig. 9. Relationship between interpolation error and downstream estimation error (SOH and SOC) across all datasets and models. Each point (circle for linear interpolation and triangle for PCHIP) corresponds to one SOC-availability case, with interpolation error averaged over the 21 features. The dashed line indicates the linear regression fit. r and ρ denote the Pearson and Spearman correlation coefficients, respectively.

evaluated datasets and experimental conditions. Currently, the framework has been validated on LFP, LMO, and NMC lithium-ion cells under the proposed pulse protocol and the practically relevant SOC range of 5%–50%. Beyond these conditions and settings, the proposed workflow can be extended to new battery cells and deployment scenarios. Such adaptation can be achieved by implementing the same feature construction and model training procedure on target-domain datasets. Specifically, the transferable component is the overall estimation workflow, while the regression models need to be retrained for the specific battery domain. Future research directions include validating this framework using more diverse datasets, evaluating its robustness under varying conditions, and extending its applications to module/pack-level state estimation.

5. Conclusion

This work addresses a practically critical but often underexplored problem in second-life battery screening: joint estimation of SOH and SOC under unknown usage histories and limited measurement budgets. The proposed framework combines short-pulse diagnostics, SOC-dependent feature construction, and data-efficient tabular learning. Specifically, 21 voltage-response features are extracted from short bipolar pulse tests and used as diagnostic descriptors for retired cells with heterogeneous chemistries, capacities, and degradation states. Based on these pulse features, both ExtraTrees and TabPFN-based ML models are developed for the estimation task. The framework is evaluated using data from 270 retired lithium-ion cells covering LFP, LMO, and NMC chemistries across four capacity classes. Under full SOC-dependent measurements for training, TabPFN achieves MAE values of 0.0076–0.0306 for SOH estimation and below 0.01 for SOC estimation across all cell groups. These results confirm that accurate state assessment of randomly retired cells can be achieved using short electrical perturbations.

To further reduce the testing burden, this work exploits the smooth but chemistry-dependent evolution of pulse-response features with SOC and reconstructs unmeasured SOC-dependent feature points using interpolation methods. Across eight SOC-availability cases, the interpolation error remains low, with average MAPE values below 0.60% for linear interpolation and below 0.39% for PCHIP. More importantly, the reduced-test results show that substantial measurement reduction can be achieved without a major loss of estimation fidelity: removing 40% of SOC-dependent pulse tests keeps the SOH MAE close to the full-measurement baseline, while even the sparsest setting, with 70% of the pulse tests removed, keeps the SOC MAE below 0.018. These findings provide practical guidelines for balancing testing cost against estimation fidelity in large-scale second-life battery screening.

CRediT authorship contribution statement

Qingbo Zhu: Writing – review & editing, Writing – original draft, Software, Methodology, Conceptualization. **Shengyu Tao:** Writing – review & editing, Supervision, Conceptualization. **Torsten Wik:** Writing – review & editing, Supervision.

Declaration of competing interest

The authors declare that they have no known competing financial interests or personal relationships that could have appeared to influence the work reported in this paper.

Acknowledgements

This work was supported by the Swedish Research Council (Grant No. 2023-04314) and the European Union's Horizon Europe programme through the Marie Skłodowska-Curie Actions (Grant Nos. 101131278 and 101283078). The authors would like to thank Prof. Changfu Zou from the Department of Electrical Engineering, Chalmers University of Technology, for valuable discussions and for proofreading the manuscript.

References

[1] Benchmark Mineral Intelligence. Global EV sales reach 20.7 million units in 2025, growing by 20%; Jan 2026 https://source.benchmarkminerals.com/article/global-ev-sales-reach-20-7-million-units-in-2025-growing-by-20 [Accessed: 3 May 2026].
[2] Global EV Outlook 2025, Tech. rep, 2025, International Energy Agency, Paris. https://www.iea.org/reports/global-ev-outlook-2025.
[3] Etxandi-Santolaya M, Canals Casals L, Corchero C. Extending the electric vehicle battery first life: performance beyond the current end of life threshold. Heliyon 2024;10(4):e26066.
[4] Lai X, Huang Y, Gu H, Deng C, Han X, Feng X, Zheng Y. Turning waste into wealth: a systematic review on echelon utilization and material recycling of retired lithium-ion batteries. Energy Storage Mater 2021;40:96–123.
[5] Ma R, Tao S, Sun X, Ren Y, Sun C, Ji G, Xu J, Wang X, Zhang X, Wu Q, et al. Pathway decisions for reuse and recycling of retired lithium-ion batteries considering economic and environmental functions. Nat Commun 2024;15(1):7641.
[6] Weng A, Dufek E, Stefanopoulou A. Battery passports for promoting electric vehicle resale and repurposing. Joule 2023;7(5):837–42.
[7] Piombo G, Niri MF, Marco J. A novel application-aware retired lithium-ion batteries regrouping approach to enable improved second life. J Clean Prod 2025;489:144526.
[8] Tao S, Liu H, Sun C, Ji H, Ji G, Han Z, Gao R, Ma J, Ma R, Chen Y, et al. Collaborative and privacy-preserving retired battery sorting for profitable direct recycling via federated machine learning. Nat Commun 2023;14(1):8032.
[9] Made RI, Lin J, Zhang J, Zhang Y, Moh LC, Liu Z, Ding N, Chiam SY, Khoo E, Yin X, et al. Health diagnosis and recuperation of aged Li-ion batteries with data analytics and equivalent circuit modeling. iScience 2024;27(4).
[10] Xu J, Sun C, Ni Y, Lyu C, Wu C, Zhang H, Yang Q, Feng F. Fast identification of micro-health parameters for retired batteries based on a simplified P2D model by using padé approximation. Batteries 2023;9(1):64.
[11] Jiang Y, Jiang J, Zhang C, Zhang W, Gao Y, Guo Q. Recognition of battery aging variations for $LiFePO_4$ batteries in 2nd use applications combining incremental capacity analysis and statistical approaches. J Power Sources 2017;360:180–8.
[12] Chen Z, Zhao W, Li W, Yu Z, Deng Y. A novel differential voltage segment-based rejection and clustering method for enhancing short and long term consistency in reuse of retired batteries. Sustain Energy Technol Assess 2025;82:104442.
[13] Wang Y, Huang H, Wang H. Rapid-regroup strategy for retired batteries based on short-time dynamic voltage and electrochemical impedance spectroscopy. J Energy Storage 2023;63:107102.
[14] Ahmeid M, Muhammad M, Lambert S, Attidekou PS, Milojevic Z. A rapid capacity evaluation of retired electric vehicle battery modules using partial discharge test. J Energy Storage 2022;50:104562.
[15] Tao S, Zhang X, Zou C. The role of machine-learning-enabled diagnostics in a circular battery economy. Chem Circ 2026;1:100005.
[16] Garg A, Yun L, Gao L, Putungan DB. Development of recycling strategy for large stacked systems: experimental and machine learning approach to form reuse battery packs for secondary applications. J Clean Prod 2020;275:124152.
[17] Qu J, Zhang B, Jiang R, Huang J, Li M, Zheng S, Yu W, Sun P, Xu Y, Hou Y, et al. Machine learning-guided multi-objective optimization for selective lithium extraction and valuable metal reuse from spent lithium-ion batteries. Chem Eng J 2025;525:169978.
[18] Neri A, Butturi MA, Gamberini R. Sustainable management of electric vehicle battery remanufacturing: a systematic literature review and future directions. J Manuf Syst 2024;77:859–74.
[19] Tao S, Moura S, Brandell D, Han Z, Urréhman S, Zou C, Zhang X, Zhou G. Artificial intelligence for battery reuse, recycling and remanufacturing. Nat Rev Clean Technol 2026;2(5):366–81.
[20] Zong B, Song Q, Min MR, Cheng W, Lumezanu C, Cho D, Chen H. Deep autoencoding Gaussian mixture model for unsupervised anomaly detection. In: Proc. Int. Conf. Learn. Represent; 2018.
[21] Zhou Z, Ran A, Chen S, Zhang X, Wei G, Li B, Kang F, Zhou X, Sun H. A fast screening framework for second-life batteries based on an improved bisecting K-means algorithm combined with fast pulse test. J Energy Storage 2020;31:101739.
[22] Ran A, Cheng M, Chen S, Liang Z, Zhou Z, Zhou G, Kang F, Zhang X, Li B, Wei G. Fast remaining capacity estimation for lithium-ion batteries based on short-time pulse test and Gaussian process regression. Energy Environ Mater 2023;6(3):e12386.
[23] Nowacki B, Ramamurthy J, Thelen A, Tischer C, Pint CL, Hu C. Rapid estimation of lithium-ion battery capacity and resistances from short duration current pulses. J Power Sources 2025;628:235813.
[24] Fahmy YA, Wang W, West AC, Preindl M. Snapshot SoC identification with pulse injection aided machine learning. J Energy Storage 2021;41:102891.
[25] Ibraheem R, Dechent P, Dos Reis G. Path signature-based life prognostics of Li-ion battery using pulse test data. Appl Energy 2025;378:124820.
[26] Gasper P, Prakash N, Knutson B, Bethel T, Ramirez-Meyers K, Condon A, Attia PM, Keyser M. Searching for a pulse: evaluating the use of rapid DC pulses for diagnosing battery health, state-of-charge, and safety. J Electrochem Soc 2025;172(6):060503.
[27] Yang Y, Biswas S, Xu R, Xiao X, Xu X, Zhang P, Gong H, Zheng X, Peng Y, Li J, et al. Capacity recovery by transient voltage pulse in silicon-anode batteries. Science 2024;386(6719):322–7.
[28] Tao S, Guo R, Lee J, Moura S, Casals LC, Jiang S, Shi J, Harris S, Zhang T, Chung CY, et al. Immediate remaining capacity estimation of heterogeneous second-life lithium-ion batteries via deep generative transfer learning. Energy Environ Sci 2025;18(15):7413–26.
[29] Lin M, Wu J, Zou J, Meng J, Wang W, Wu J. Retired battery screening based on Markov transition field and swin transformer. IEEE Trans Transp Electrif 2023;10(2):4217–27.
[30] Zhang Y, Wik T, Bergström J, Zou C. State of health estimation for lithium-ion batteries under arbitrary usage using data-driven multimodel fusion. IEEE Trans Transp Electrif 2023;10(1):1494–507.
[31] Yuan Y, Jiang B, Chen Q, Wang X, Wei X, Dai H. A comparative study of battery state-of-charge estimation using electrochemical impedance spectroscopy by different machine learning methods. Energy 2025;328:136658.
[32] Bao G, Liu X, Zou B, Yang K, Zhao J, Zhang L, Chen M, Qiao Y, Wang W, Tan R, et al. Collaborative framework of transformer and LSTM for enhanced state-of-charge estimation in lithium-ion batteries. Energy 2025;322:135548.
[33] Fritsch FN, Butland J. A method for constructing local monotone piecewise cubic interpolants. SIAM J Sci Stat Comput 1984;5(2):300–4.
[34] Geurts P, Ernst D, Wehenkel L. Extremely randomized trees. Mach Learn 2006;63(1):3–42.
[35] Mastelini SM, Nakano FK, Vens C, de Leon Ferreira ACP, et al. Online extra trees regressor. IEEE Trans Neural Netw Learn Syst 2022;34(10):6755–67.
[36] Hollmann N, Müller S, Purucker L, Krishnakumar A, Körfer M, Hoo SB, Schirrmeister RT, Hutter F. Accurate predictions on small data with a tabular foundation model. Nature 2025;637(8045):319–26.
[37] Liu H, Li C, Hu X, Li J, Zhang K, Xie Y, Wu R, Song Z. Multi-modal framework for battery state of health evaluation using open-source electric vehicle data. Nat Commun 2025;16(1):1137.
[38] Yang F, Zhang S, Li W, Miao Q. State-of-charge estimation of lithium-ion batteries using LSTM and UKF. Energy 2020;201:117664.
[39] Bian X, Zou C, Fridholm B, Sundvall C, Wik T. Smart sensing breaks the accuracy barrier in battery state monitoring. Energy Storage Mater 2025;80:104410.
[40] Tao S, Ma R, Zhao Z, Ma G, Su L, Chang H, Chen Y, Liu H, Liang Z, Cao T, et al. Generative learning assisted state-of-health estimation for sustainable battery recycling with random retirement conditions. Nat Commun 2024;15(1):10154.